Article

Graphene-enabled laser lift-off for ultrathin displays

Sumin Kang [1], Jaehyeock Chang [2], Jaeseung Lim[3,4], Dong Jun Kim[5], Taek-Soo Kim [5], Kyung Cheol Choi [2], Jae Hak Lee [3] & Seungman Kim [3,4,6] ✉

Laser lift-off (LLO) of ultrathin polyimide (PI) films is important in the manufacturing of ultrathin displays. However, conventional LLO technologies face challenges in separating the ultrathin PI films without causing mechanical and electrical damage to integrated devices. Here, we propose a graphene-enabled laser lift-off (GLLO) method to address the challenges. The GLLO method is developed by integrating chemical vapor deposition (CVD)-grown graphene at the interface between a transparent carrier and an ultrathin PI film, exhibiting improved processability and lift-off quality. In particular, the GLLO method significantly mitigates plastic deformation of the PI film and minimizes carbonaceous residues remaining on the carrier. The role of graphene is attributed to three factors: enhancement of interfacial UV absorption, lateral heat diffusion, and adhesion reduction, and experimentations and numerical simulations verify the mechanism. Finally, it is demonstrated that the GLLO method separates ultrathin organic light-emitting diode (OLED) devices without compromising performance. We believe that this work will pave the way for utilizing CVD graphene in various laser-based manufacturing applications.

Since the discovery of a laser ablation-driven separation phenomenon in organic polymers[1], the laser lift-off (LLO) process has been widely utilized in the manufacturing of flexible electronics[2,3]. Among various LLO-processable polymers, polyimide (PI) is considered the most suitable substrate material for fabricating flexible displays owing to its superior thermal stability[4]. In this regard, the bendable and rollable characteristics have been demonstrated using PI films with thicknesses ranging from 10 to 100 μm[5–7]. Meanwhile, in stretchable display applications, the reduction of the thickness of PI films is advantageous for enhancing stretchability and mechanical reliability[8,9]. Moreover, next-generation applications, such as implantable and wearable photonic healthcare devices[10–12], require the use of ultrathin (sub-5 μm) substrate thickness to allow conformal contact onto soft and

curvilinear surfaces based on their extreme flexibility[13]. However, the extreme flexibility renders the PI films delicate to mechanical deformation during the LLO process, causing wrinkling and rupturing that can result in the malfunction of photonic devices.

Two representative approaches have been developed to reduce laser-induced damage on the PI films during the LLO process. The first approach is placing a sacrificial layer, including amorphous gallium oxide (α-GaO$_x$), amorphous silicon (α-Si), and lead zirconate titanate (PZT), between a PI film and a glass carrier[5,14,15]. Although these sacrificial layers reduced thermal damage to flexible substrates and thin-film devices[16,17], significant mechanical deformation during the LLO process still hinders the successful lift-off of the ultrathin PI films[15]. In addition, the deposited sacrificial layer cannot be reused after the LLO

[1]Department of Mechanical and Automotive Engineering, Seoul National University of Science and Technology, Seoul, Republic of Korea. [2]School of Electrical Engineering, Korea Advanced Institute of Science and Technology, Daejeon, Republic of Korea. [3]Semiconductor Manufacturing Research Center, Korea Institute of Machinery and Materials, Daejeon, Republic of Korea. [4]Department of Robot·Manufacturing Systems, University of Science and Technology, Daejeon, Republic of Korea. [5]Department of Mechanical Engineering, Korea Advanced Institute of Science and Technology, Daejeon, Republic of Korea. [6]Wm Micheal Barens'64 Department of Industrial and Systems Engineering, Texas A&M University, College Station, TX, USA. ✉e-mail: kimsm@kimm.re.kr

process, leading to an increase in manufacturing costs. The second approach is the direct ablation of the PI films by controlling laser irradiation parameters, such as multiple irradiations of low-fluence laser[13,18] and optimization of laser type and beam shape[19]. These methods enabled the reduction of the plastic deformation during the LLO process, but achieving successful separation of the ultrathin PI film with a low-fluence and single-pass LLO process, which facilitates high-throughput manufacturing, remains challenging[13].

In this paper, we hypothesize that chemical vapor deposition (CVD)-grown graphene, a large-area processable 2D nanostructured carbon material, is advantageously utilized in the LLO process owing to its unique optical, thermal, adhesion, and geometrical characteristics[20–22]. Specifically, the high in-plane thermal conductivity, UV absorptivity, and lubricating property can result in laser ablation without thermal and mechanical damage. Moreover, CVD graphene enables not only large-area integration but also the programming of the LLO performance by controlling the number of integrated layers. Based on these hypotheses, a graphene-enabled laser lift-off (GLLO) method was developed by integrating the graphene layer at the interface between an ultrathin PI film and a glass carrier. The process window and lift-off quality of the PI film for the conventional LLO and GLLO methods were compared to demonstrate the effectiveness of the integrated graphene, and the role of graphene layers during the ablation process was elucidated by thorough experimentations and numerical simulations. Furthermore, the applicability of the GLLO method was verified by demonstrating ultrathin organic light-emitting diode (OLED) devices.

Results

GLLO process
Figure 1 illustrates the procedures and characteristics of the GLLO and conventional LLO methods. The primary distinction between the two methods is the insertion of CVD-grown graphene at the interface between a transparent glass carrier and a PI film. The procedure of the GLLO method is depicted in Fig. 1a. The glass carrier–graphene–PI film structured specimen was prepared by transferring the graphene layer onto the carrier and spin coating the PI film. In this process, the graphene layer was transferred layer-by-layer using a roll-to-roll manner, controlling the number of integrated layers (Supplementary Fig. 1). The thickness of the spin-coated PI film, the target lift-off material, was fixed at 2.9 μm (Supplementary Fig. 2), which is significantly thinner

than the reported thickness in previous LLO studies[5–7,13–15,18,19]. In this regard, the presence of graphene layers on the glass carrier does not significantly influence the thickness of the fabricated PI films (Supplementary Fig. 3). Detailed information on specimen preparation is provided in the Methods section. After specimen preparation, a 355 nm diode-pumped solid-state (DPSS) laser system was utilized for the lift-off process (Supplementary Fig. 4). The DPSS layer system offers advantages in cost-competitiveness, high reliability, and beam quality for precision manufacturing compared to excimer laser systems. Consequently, the integrated graphene layer enabled the successful lift-off of the 2.9 μm-thick PI film without significant plastic deformation and carbonaceous PI residues.

In a comparative experiment, the conventional LLO process was conducted using the specimen composed of the glass carrier and 2.9 μm-thick PI film, which is identical to the GLLO method, except for the absence of the graphene layer (Fig. 1b). In this case, achieving the successful lift-off of the ultrathin PI film proved to be highly challenging. For example, partial separation of the PI film was observed under low laser fluence conditions, while micro-scale wrinkles or ruptures occurred under high laser fluence conditions. Moreover, the conventional LLO method resulted in thick carbonaceous PI residues remaining after the process, impeding the recycling of the expensive glass carrier.

Process window and lift-off quality of GLLO process
The process window and lift-off quality of both the GLLO and conventional LLO methods were investigated (Fig. 2). The LLO process was performed by irradiating a UV laser pulse onto the glass carrier–graphene–PI film specimen (Fig. 2a). In this experiment, two parameters, laser fluence and scanning pitch, were controlled within the ranges of 63.4–158.5 mJ/cm² for the laser fluence and 7.5–150 μm for the scanning pitch. Detailed experimental setup for the laser system is described in the "Methods" section. The lift-off area was controlled to 1.5 × 1.5 mm² for investigating the LLO performance, and for the GLLO process, the specimens integrated 4 layers of graphene. The results of each LLO process were categorized into partial separation, wrinkling, rupturing, and successful lift-off. The criterion for the successful lift-off is defined as the separation of the PI films without microscale wrinkles, ruptures, and partially bonded areas. Detailed explanations and representative images for each classification are provided in Supplementary Fig. 5.
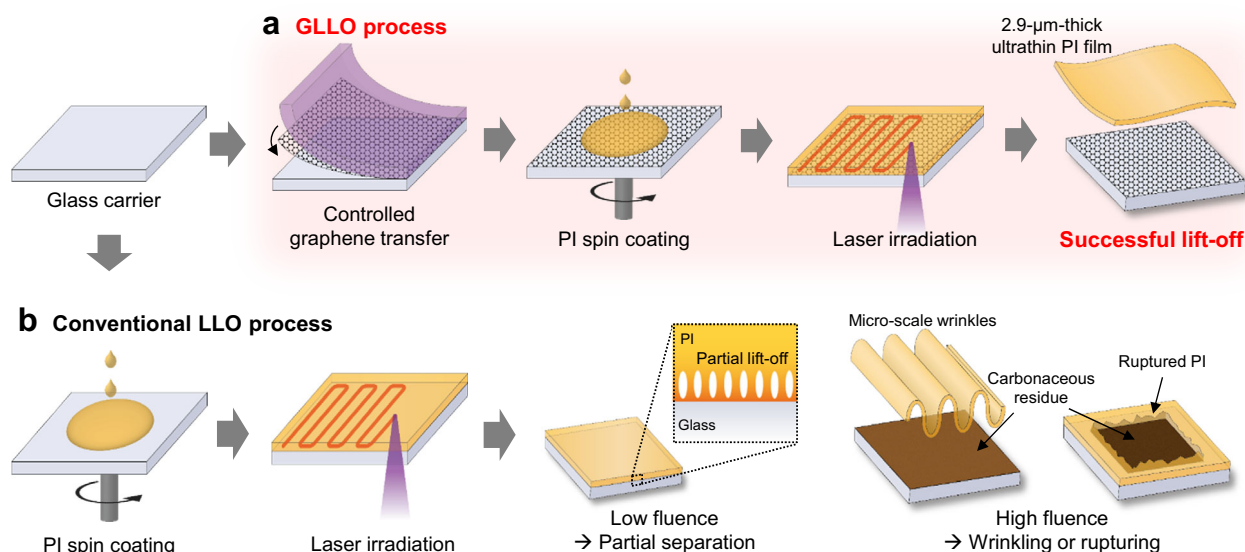

Fig. 1 | Schematic illustration of the procedures and characteristics of the presented and conventional laser lift-off methods for separating the ultrathin polyimide (PI) film. a Graphene-enabled laser lift-off (GLLO) process. **b** Conventional laser lift-off (LLO) process.
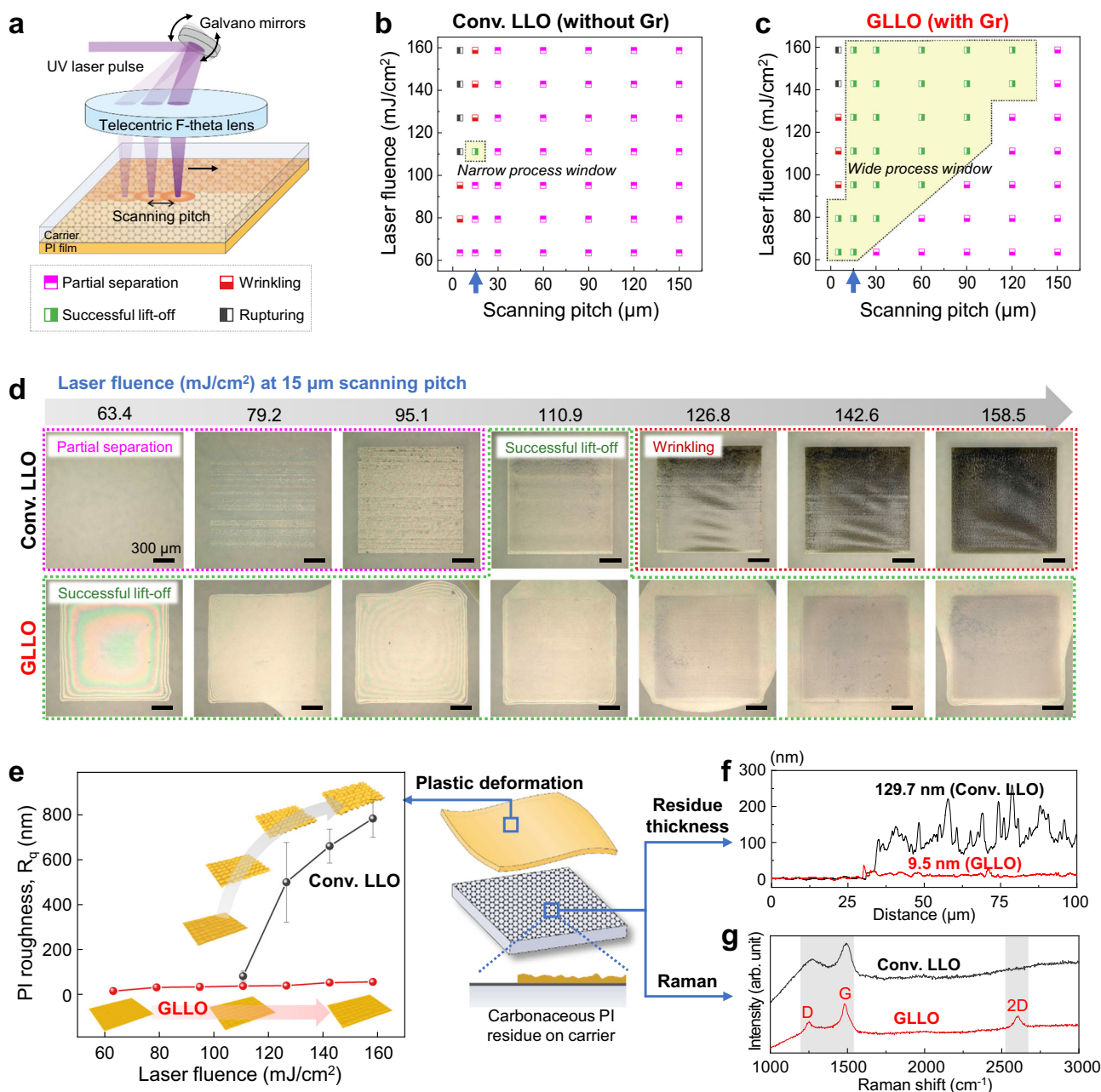
Fig. 2 | Performance of the conventional LLO and GLLO methods. a Schematic illustration of the lift-off process of the ultrathin PI film with ultraviolet (UV) laser irradiation. The process results were categorized into partial separation (pink, upper half-filled symbol), wrinkling (red, lower half-filled symbol), successful lift-off (green, right half-filled symbol), and rupturing (black, left half-filled symbol) (**b**, **c**) Lift-off results with respect to laser fluence and scanning pitch for (**b**) conventional LLO and (**c**) GLLO methods. The green areas represent process windows for successful lift-off. **d** Optical microscopy (OM) images of PI films after the lift-off process for each laser fluence with a fixed scanning pitch of 15 μm. The images in the first and second rows correspond to the conventional LLO and GLLO methods,

respectively. Scale bars: 300 μm. **e** Surface roughness of the free-standing PI films separated with the conventional LLO and GLLO methods for each laser fluence. Inset images display the 3D surface topographies of the PI films (scale factor: 5). Error bars represent standard deviations obtained from samples ($n \geq 8$). **f** The measured thickness of carbonaceous residues on the glass carriers, and (**g**) Raman spectra analyzed on the glass carriers after each process. The shaded region highlights the differences in Raman peaks between the graphene-integrated thin residue from the GLLO method and the thick residue from the conventional LLO method.

Figure 2b displays the lift-off results of the conventional LLO process without the introduction of graphene layers. The results highlight that the process window for successful lift-off is very narrow. At a scanning pitch of 15 μm (indicated by the blue arrow in Fig. 2b), only one condition, a laser fluence of 110.9 mJ/cm², successfully separated the ultrathin PI film without inducing significant wrinkles. In other cases, laser fluences lower than 110.9 mJ/cm² resulted in partial separation, while higher fluences led to wrinkling in the separated PI

film due to plastic deformation during the ablation process. The optical microscopy (OM) images in the first row of Fig. 2d verify the aforementioned lift-off behavior. More detailed analysis on the lift-off results using the conventional LLO method is provided in Supplementary Fig. 6.

In contrast, the GLLO process exhibited a wide process window for successful lift-off (Fig. 2c). When considering the scanning pitch of 15 μm (indicated by the blue arrow in Fig. 2c), all laser fluences ranging

from 63.4 to 158.5 mJ/cm^2 successfully separated the ultrathin PI film without significant damage. The OM images in the second row of Fig. 2d demonstrate the successful lift-off results, leading to moiré fringes under low laser fluence conditions[23]. OM images of the other specimens after the conventional LLO and GLLO processes are shown in Supplementary Figs. 7 and 8, respectively, highlighting apparent differences between the lift-off results of the GLLO and conventional LLO methods. Furthermore, the effectiveness of the GLLO method in reducing damage during the lift-off process was also confirmed in different material systems, indicating the method's expandability (Supplementary Figs. 9 and 10).

In addition to macro- and micro-scale observations, we explored nanoscale characteristics of the LLO methods. First, the surface roughness of the free-standing PI film was measured by confocal microscopy to analyze the amount of plastic deformation during the ablation process (Fig. 2e). When the laser fluence was controlled with a fixed scanning pitch of 15 μm, the surface roughness of the PI film separated by the conventional LLO process sharply increased as the laser fluence increased, whereas the GLLO method dramatically reduced the surface roughness of the PI film and its increasing rate with respect to the laser fluence. These results indicate that the laser-induced plastic deformation during the ablation process significantly reduced owing to the presence of graphene layers, and this reduction allows for the demonstration of damage-free separation of ultrathin devices. Additionally, the plastic deformation was also reduced even in thicker PI films by the GLLO method, although the differences were mitigated under lower fluence conditions due to the third-power relationship between bending stiffness and film thickness (Supplementary Fig. 11). Moreover, it was observed that the graphene layer still enabled the lift-off process of thicker PI films at a significantly lower laser fluence of 63.4 mJ/cm^2.

Second, the glass carrier was investigated after the lift-off processes. Figure 2f illustrates the thicknesses of remaining carbonaceous PI residues on the carrier measured by a stylus profiler. The measurements were taken from specimens separated at laser fluences of 63.4 and 110.9 mJ/cm^2 with a scanning pitch of 15 μm for the GLLO and conventional LLO methods, respectively, as they are the minimum fluence conditions for the complete separation of the ultrathin PI film in each case. The results reveal that the average thickness of PI residues with the conventional LLO method is 129.7 nm, similar to a previous study[19], while the GLLO method enables a remarkable reduction in thickness to 9.5 nm. Moreover, the Raman spectrum of a GLLO-processed carrier shows G and 2D graphene peaks[24] combined with a thin carbonaceous PI residue, indicating the presence of graphene layers after the GLLO process. In contrast, the Raman spectrum of a conventional-LLO-processed carrier displays a typical Raman spectrum of carbonaceous PI residues[25]. The remaining graphene on the carrier represents the potential for recycling the graphene-integrated glass carrier in device fabrication.

Role of integrated graphene

We investigated the role of the CVD graphene layer in the laser-induced ablation process to elucidate the experimentally observed significant differences between the GLLO and conventional LLO methods. Figure 3a illustrates the ablation mechanism of the conventional LLO method. When the UV laser is irradiated, ablation of PI occurs within the PI film near the glass carrier–PI interface. The ablation of PI is typically attributed to the photothermal decomposition of the material with a vertically distributed narrow pyrolysis zone[26]. Moreover, as a result of photothermal decomposition, gaseous products are produced inside the PI film, separating the PI films. In particular, the vertically distributed pyrolysis zone results in the initial formation of a sharp blister, and the gaseous products further expand the sharp blister vertically, resulting in high height and low diameter (Fig. 3b). At this point, the intrinsically strong interfacial adhesion[27,28]

between the glass carrier and PI film hinders lateral crack growth into glass–PI interface. Consequently, the high mechanical strain associated with the expansion of the sharp blister causes plastic deformation of the PI film[29,30].

The role of the graphene layer is attributed to three effects: (1) enhancement of UV absorption at the interface, (2) lateral diffusion of heat, and (3) reduction of interfacial adhesion (Fig. 3c). First, the graphene layer enhances the absorption of photothermal energy at the interface, relocating the ablation sites from within the PI film to the graphene–PI interface. This relocation contributes to the reduction of the thickness of carbonaceous residue. Second, the high in-plane thermal conductivity of the graphene layer effectively disperses the absorbed photothermal energy in the horizontal direction, thereby widening the narrow pyrolysis zone. These two factors, the enhancement of interfacial absorption and lateral heat diffusion, enable the smoothing of the initially generated blister by distributing the pyrolysis zone horizontally. Third, the graphene layer reduces the interfacial adhesion of the PI film by hindering molecular interactions between the glass carrier and the PI film. Owing to the low adhesion, the generated gaseous products are propagated to graphene–PI interface, leading to lateral interfacial crack growth and further increasing the blister diameter (Fig. 3d). The resulting smooth blister, with low height and high diameter, reduces the mechanical strain during the ablation process, allowing the lift-off of the ultrathin PI film without significant damage. More detailed separation and deformation processes of the PI film for the conventional LLO and GLLO methods are described in Supplementary Fig. 12, and cross-sectional images of the blisters observed via focused ion beam (FIB)-scanning electron microscopy (SEM) are provided in Supplementary Fig. 13.

According to the explanations, the shape of the blister is the key difference between the conventional LLO and GLLO methods. Therefore, we investigated the blister shape by irradiating a single UV laser pulse to the specimens with different numbers of graphene layers, and experimentally measuring the blister geometry using confocal microscopy (Fig. 3e, f). In this regard, the number of graphene layers and laser fluence were controlled from 0 to 4 layers and 23.8–110.9 mJ/cm^2, respectively. The results show that, under laser fluence conditions exceeding 100 mJ/cm^2, there were significant differences in the blister height among the specimens without graphene, with single-layer graphene, and with multilayer graphene (Fig. 3e). In addition, the blister diameter almost proportionally increased as the number of graphene layers increased (Fig. 3f). The reduction in blister height and the enlargement of blister diameter with the addition of graphene layers verify the effect of the graphene layers on the smoothing behavior of blisters as depicted in Fig. 3d. The representative shapes of blisters formed at the 110.9 and 79.2 mJ/cm^2 laser fluence conditions are represented in Fig. 3g. Moreover, it was found that the threshold laser fluence required to form a blister decreased as the number of graphene layer increased. This behavior is attributed to the enhanced UV absorption at the graphene layers, which increases the maximum temperature driven by photothermal energy under the same laser fluence conditions.

The suggested three effects of graphene during the ablation process were validated through experiments and numerical simulations. Figure 4a represents the UV-Vis absorption spectrum for varying numbers of graphene layers. The results demonstrate the exceptional absorptivity of the graphene layer in the UV region wavelength. In particular, the absorbance at the 355 nm wavelength, employed in the lift-off experiments, exhibited nearly linear growth with the addition of graphene layers, rising from 0.035 to 0.132. This validates the characteristic of UV absorption enhancement. The peel test results in Fig. 4b also confirm that the graphene layer significantly reduced the interfacial adhesion by impeding molecular interactions between the glass carrier and the PI film. In particular, the presence of a single graphene layer remarkably reduced the interfacial adhesion similar to
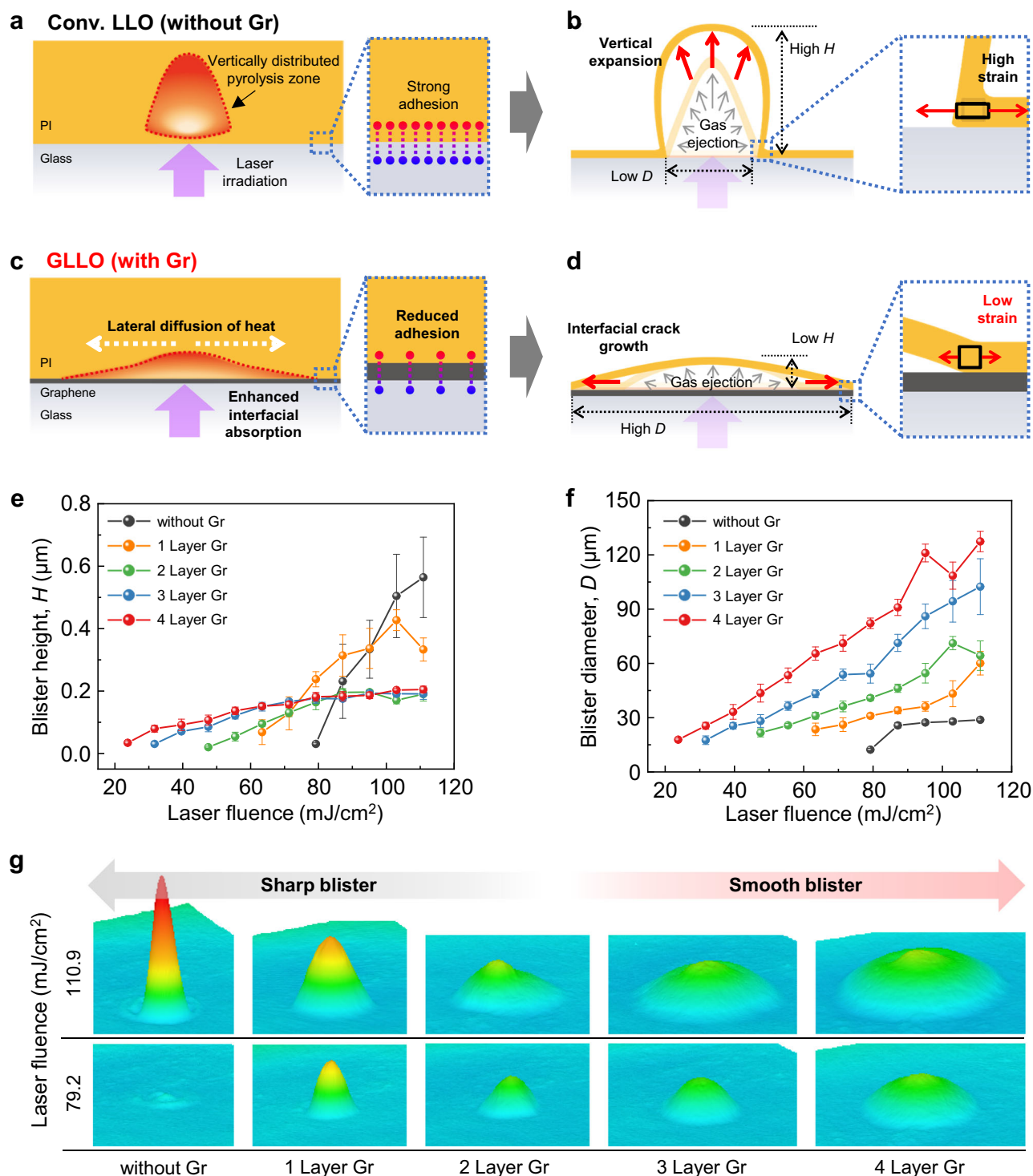
Fig. 3 | The role of the graphene layer and blistering behavior during the ablation process. a Ablation mechanism of the conventional LLO method, and (**b**) the resulting blister shape with high height and low diameter. The sharp blister introduces high mechanical strain. **c** The role of the graphene layer during the ablation process of the GLLO method, and (**d**) the resulting blister shape with low height and high diameter. The smooth blister enables the reduction of mechanical strain. **e**, **f** Measured (**e**) height and (**f**) diameter of blisters with respect to the laser fluence and the number of graphene layers. Error bars represent standard deviations obtained from samples ($n = 7$). **g** The representative images of blisters at the laser fluence of 110.9 and 79.2 mJ/cm^2 (scale factor: 120). The shape and dimension of the blisters were experimentally measured using confocal microscopy.

that of multilayered graphene. However, there was an obvious distinction in the blister height and diameter with the addition of the graphene layer as shown in Fig. 3e, f. Accordingly, it can be concluded that the enhancement of UV absorption and lateral heat diffusion, which are related to the photothermal decomposition of the PI film,

are important in explaining the ablation behavior. Moreover, the relative differences in temperature profiles during the ablation process, concerning the number of graphene layers, were visualized through finite element analysis (FEA) simulation (Fig. 4c). In this regard, due to the different thickness scales of the materials, the
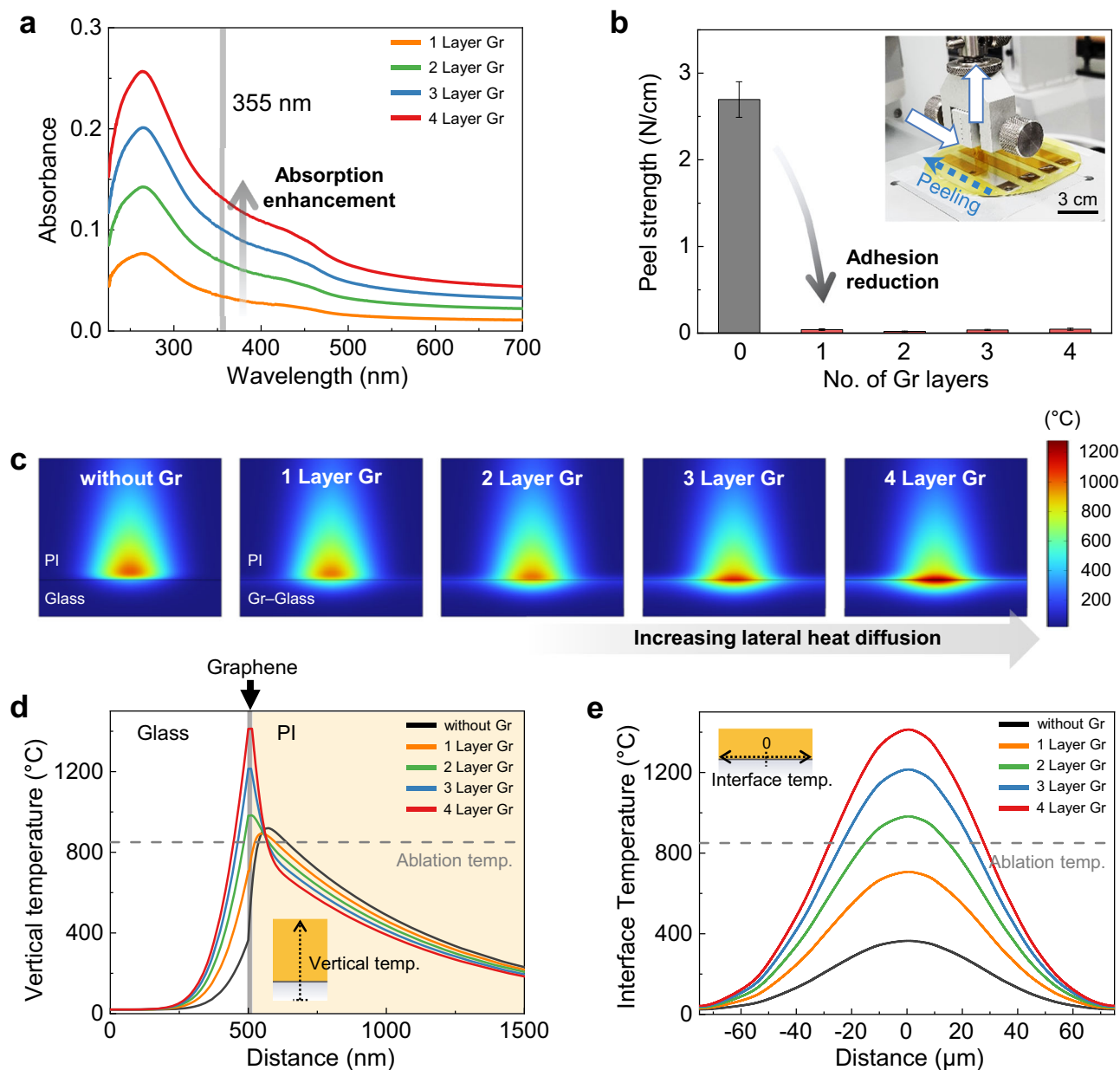
Fig. 4 | Verification of the mechanism. a UV-Vis absorption spectrum of each graphene layer. **b** Peel strength of the fabricated PI film for the number of underlying graphene layers. Error bars represent standard deviations obtained from samples ($n = 4$). The inset shows the experimental setup. **c** Temperature profiles during the ablation process for the number of graphene layers. The profile results were obtained using the reduced simulation model. **d**, **e** Temperature distributions (**d**) in the vertical direction and (**e**) at the glass(graphene)–PI interface. The distribution results were obtained using the full-scale simulation model. Insets illustrate the directions for temperature data extraction in the simulation model, and gray dashed lines represent the threshold ablation temperature. The colored regions in (**d**) indicate the variation in materials along the vertical distance.

simulation model with a reduced scale was introduced for the visualization (Supplementary Fig. 14). Detailed information on the FEA simulation is provided in the "Methods" section. The results illustrate that the performance of lateral diffusion of absorbed photothermal energy significantly improved as the number of graphene layers increased. These analyzes provide reasonable evidence for the role of graphene in the GLLO process.

Further investigations were conducted using a full-scale simulation model (Supplementary Fig. 15), to examine the actual temperature distributions in both the vertical direction and at the interface (Fig. 4d, e). The results reveal a significant variation in the maximum temperature between cases with multilayered and without graphene. Especially, in the case of the 4-layered graphene, the maximum

temperature was observed at the graphene–PI interface, whereas in the absence of graphene, it was located 87 nm above the interface. This distinction is attributed to the enhanced light-absorbing characteristics at the graphene–PI interface due to the graphene layers, and it is related to the reduction of the thickness of carbonaceous residues. The light-absorbing characteristics and the absorption fractions with respect to the number of graphene layers are illustrated in Supplementary Figs. 16 and 17, respectively.

In addition, taking into account the threshold ablation temperature of 850 °C for the PI films[31], it can be inferred that the ablation occurs at the interior region of the PI film with a diameter of 22 µm in a typical LLO process. In contrast, the multilayered graphene relocates the ablation region to the interface with a diameter of 55.6 µm
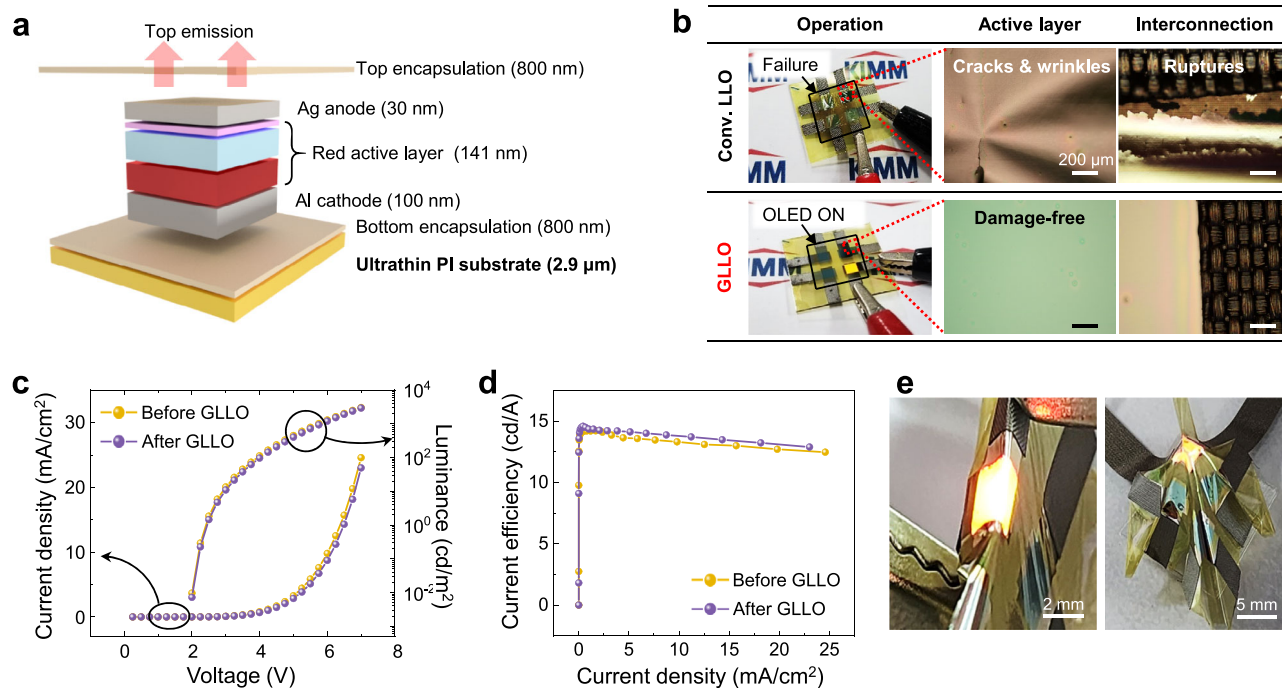
Fig. 5 | Application of the GLLO method to ultrathin organic light-emitting diode (OLED) devices. a Schematic illustration of the OLED structure. **b** Photographs and OM images comparing the lift-off results between the conventional LLO and GLLO methods. Scale bars: 200 μm. **c, d** Electrical performance of the fabricated OLEDs before and after the GLLO process: (**c**) current density-voltage-luminance properties and corresponding (**d**) current efficiency-current density curve. **e** Operation of the OLEDs under severe mechanical deformations.

(Supplementary Fig. 18). The results can underpin the notion of lateral crack growth by considering that experimentally obtained blister diameters of the GLLO method presented in Fig. 3f are larger than the simulation-based ablation diameter. Furthermore, the effect of graphene on the thermal protection of a device layer during the lift-off process was investigated by analyzing the temperature distributions. The results demonstrate that the graphene layers can contribute to reducing the maximum temperature of the device layer on thinner PI films, by increasing UV light absorption at the interface and dispersing the heat in a lateral direction during the GLLO process (Supplementary Fig. 19).

Applicability to ultrathin displays

Finally, the applicability of the GLLO method to ultrathin displays was investigated by using OLEDs fabricated on the 2.9 μm-thick ultrathin PI substrate. Figure 5a illustrates the OLED structure, consisting of an Al cathode, red active layer, and Ag anode layer, with encapsulation layers on both top and bottom. In particular, the encapsulation layers were fabricated using an organic-inorganic hybrid nano-stratified structure to ensure mechanical reliability[32,33]. Detailed information on the fabrication of OLEDs and encapsulation layers is provided in the "Methods" section. After the fabrication of the OLEDs on the ultrathin PI substrate, the PI substrate was separated using the conventional LLO and GLLO methods. In this process, laser fluences of 110.9 and 63.4 mJ/cm² were applied in the conventional LLO and GLLO processes, respectively, with a scanning pitch of 15 μm. These conditions were chosen because they succeeded in completely separating the ultrathin PI film (Fig. 2d). As a result, notable differences in the lift-off results were observed between the two methods (Fig. 5b). The OLED devices separated using the conventional LLO method experienced malfunctions due to the high plastic deformation, resulting in cracking and wrinkling in the active layer, as well as rupturing in interconnection regions. In contrast, the GLLO method enabled the successful lift-off and operation of the

ultrathin OLED devices without damage owing to the presence of graphene layers.

The current density-voltage-luminance properties of the fabricated OLEDs were investigated before and after the GLLO process (Fig. 5c). The as-fabricated OLEDs on the PI substrate and after lift-off process showed sharp increases in current density, and their turn-on voltages, extracted at the luminance value of 1 cd/m², were almost identical at approximately 2.4 V. At an applied voltage of 7 V, the fabricated OLEDs before and after GLLO process exhibited current density values of 24.58 and 23.01 mA/cm², respectively, with corresponding luminance values of 3066 and 2967.2 cd/m². Moreover, the current efficiency values of the OLEDs were maintained above 12.5 cd/A in both cases (Fig. 5d). These results indicate that the GLLO process separated the OLED devices without compromising electrical performance, beyond just avoiding mechanical damage. Figure 5e demonstrates that the OLEDs on the ultrathin PI substrate can operate under severe mechanical deformations, such as twisting in a folded state and conformally contacting with a sharp object.

Furthermore, the reusability of the graphene-integrated glass carrier was investigated by repeating the processes of spin coating the 2.9 μm-thick ultrathin PI substrate, OLED fabrication, and GLLO sequentially (Fig. 6a). The OLEDs fabricated in the first cycle were separated with a laser fluence of 63.4 mJ/cm². Consistent with the results in Fig. 5, the devices maintained their current density-voltage-luminance properties and current efficiency before and after the GLLO process (Fig. 6b, c). The reusability of the graphene-integrated glass carrier was evaluated by considering the electrical performance variation of OLEDs fabricated on reused carriers. In this regard, delamination of the OLEDs in the second and third fabrication cycles required a slightly higher laser fluence of 79.2 mJ/cm² for complete lift-off. Moreover, the analysis results indicate that although the OLEDs remained operational after the GLLO process, a slight degradation in luminance was observed (Fig. 6b). We carefully anticipate that the higher laser fluence requirement and degraded luminance resulted
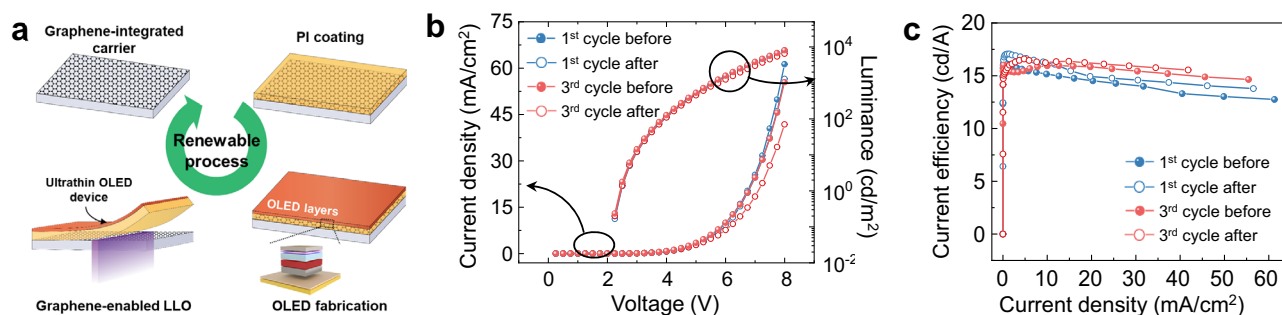
Fig. 6 | Reusability of the graphene-integrated carrier. a Schematic illustration of the renewable process of the graphene-integrated carrier. **b, c** Electrical performance variation of the OLEDs fabricated in the first and third cycles, before and after the GLLO process. **b** current density-voltage-luminance properties and corresponding (**c**) current efficiency-current density curve.

from the thin carbonaceous PI residues represented in Fig. 2f. In other words, the thin residues covered the integrated graphene layer, hindering the reduction of interfacial adhesion of newly coated PI substrates and increasing the distance from the graphene layer. Therefore, more effort will be needed to completely remove the carbonaceous residues, ensuring the intact reusability of the graphene-integrated carrier.

Discussion

This paper presented the significant influence of CVD-grown graphene on the LLO process. The role of graphene layers in the GLLO process was divided into three factors: enhancement of UV absorption at the interface, lateral diffusion of heat, and adhesion reduction. These factors changed the blistering behaviors, consequently reducing plastic deformation during the ablation process. The suggested mechanism was validated by experimental and numerical investigations. The discussion on the performance and applicability of the GLLO method is presented below.

In terms of performance, the GLLO method achieved successful lift-off of the significantly thinner PI films than the previous LLO studies[5–7,13–15,18,19], offering a wide process window and minimal plastic deformation. Moreover, the GLLO method requires only a single pass irradiation of a low fluence laser with a wide scanning pitch owing to the graphene layer, enabling higher throughput processes compared to the previously reported multiple irradiations of low fluence lasers. Meanwhile, the photonic lift-off (PLO) method, which employs high-intensity light pulses of flash lamps instead of lasers and relatively thick metallic light-absorbing layers such as Mo and W/Ti alloys, also enables high throughput processes[34–37]. However, the required light energy density of the PLO processes is much higher than that of the LLO processes. This higher light energy density potentially causes damage to sub-10 μm PI films with typical molecular structures[34], and integrated devices composed of brittle electrodes and encapsulation layers[35]. Considering these characteristics, it can be concluded that the GLLO method allows for high throughput and precision lift-off of ultrathin PI films.

Regarding the applicability of the GLLO method, it was demonstrated that OLEDs fabricated on the 2.9 μm-thick PI substrate were successfully separated without mechanical damage and electrical performance degradation, which is a challenging feat for conventional LLO methods. Concerning the reusability of the graphene-integrated carrier, the separation of ultrathin OLED devices fabricated on reused carriers was achieved with a slightly higher laser fluence irradiation. Although the experiment demonstrated early-stage reusability, a slight degradation in OLED luminance was observed after the GLLO process. This degradation in LLO performance may be attributed to the remaining thin carbonaceous PI residues on the carrier, which cover the graphene layers. It is anticipated that further study is required for

the complete reusability of the graphene-integrated carrier, even though the presented GLLO method reduced the thickness of carbonaceous PI residues by approximately 92.8% compared to the conventional LLO methods. Several endeavors, such as optimization of laser irradiation conditions and beam profiles, and advances in interlayer materials, will be worthwhile for enhancing LLO performance, reusability, and industrial applicability. Finally, we believe that this work will open up new possibilities for utilizing CVD-grown graphene in laser-based manufacturing applications, such as emerging displays, wafer-level packaging, and energy-harvesting devices.

Methods

Transfer of CVD-grown graphene

Large-area CVD-grown graphene on thermal release tape (Graphene-Lab Co., Ltd) was utilized to integrate graphene layers onto a 500 μm-thick glass carrier (Eagle XG, Corning Inc.). Before transferring the graphene layers, the glass carrier underwent cleaning with acetone, isopropyl alcohol, and deionized water in sequence, followed by drying with a flow of nitrogen gas. The roll-to-roll transfer process was conducted by inserting the graphene layer and glass carrier together between two heated rollers, which have a mild temperature of 150 °C. Multilayered graphene integration was achieved by repeating the roll-to-roll process on the same substrate. The quality of integrated graphene layers is represented in Supplementary Fig. 20.

Fabrication of ultrathin PI film

The ultrathin PI film was fabricated on the graphene-integrated glass carrier by the following procedure. A solution of PI (VTEC PI 1388, Richard Blaine International Inc.) was carefully dispensed onto the carrier and then spin-coated at 5000 rpm for 40 seconds. The uncured PI underwent subsequent soft-baking at 120 °C for 30 minutes, followed by hard-baking at 300 °C for 30 minutes on a hotplate. The cured PI film was gradually cooled down to room temperature. After fabrication, the thickness of the PI film was measured using a stylus profiler and confocal microscopy.

Laser and optical system

To irradiate the laser beam onto the prepared specimen, we utilized a DPSS laser (DX-355-15, Photonics Industries) with a wavelength of 355 nm as the laser pulse source. The pulse repetition rate was set at 50 kHz with a duration of 14 ns. The pulse had a Gaussian profile (Supplementary Fig. 21), and its spot size was adjusted to 56.7 μm (full width at half maximum) using an optical system that contains power and polarization control. To focus the pulse on the specimen plane and control the scanning pitch, the Gaussian energy distribution laser pulse was inserted into a 2D laser scanner (hurrySCAN III 10, Scanlab) which includes a telecentric f-theta lens with a focal length of 160 mm. These LLO experiments were conducted in a cleanroom environment

where the temperature and relative humidity were controlled at 22 °C and 40%, respectively, under ambient air conditions.

FEA simulation

The numerical simulation was performed to analyze the temperature distribution during the ablation process using the light-absorbing heat transfer module of the commercial FEA software COMSOL. In the simulation model, a glass–graphene–PI structure was created, and the properties of each material were assigned based on the references[26,38–41]. In particular, the thickness of the graphene layer was set to 0.335 nm for the reduced model in Supplementary Fig. 14, and 3.35 nm for the full-scale model in Supplementary Fig. 15 due to limitations in mesh generation. Considering the thickness differences, the equivalent absorption coefficient of graphene was assigned using measured absorbance and the Beer-Lambert law. The material properties are represented in Supplementary Table 1. The irradiated laser pulse was set to a fluence of 158.4 mJ/cm^2 and a duration of 14 ns, with a Gaussian profile having a standard deviation of 20 nm for the reduced model and 24.076 μm for the full-scale model.

Fabrication of OLEDs

The top-emitting red OLEDs were fabricated on the bottom-encapsulated PI substrate by thermal evaporation. The red OLEDs were deposited with the following structure in sequence: Al (100 nm)/Liq (1 nm)/Bebq$_2$:Ir(piq)$_3$ (70 nm, 8 wt%)/NPB (65 nm)/MoO$_3$ (5 nm)/Ag (30 nm). Al was used as a cathode, and 8-quinolinolato-lithium (Liq) was used as an electron injection layer. Then, the host material bis(10-hydroxybenzo(h)quinolinato)beryllium complex (Bebq$_2$) and the red emission dopant tris(1-phenylisoquinoline)iridium (Ir(piq)$_3$) were co-deposited for an emitting layer. N, N0 diphenyl-N, N0-bis (1,10-biphenyl)−4,40-diamine (NPB) was used as a hole-transporting layer. Finally, MoO$_3$ was deposited as a hole injection layer, and Ag served as a transparent anode. After OLED deposition, a layer of Kapton tape was attached to the end part of the electrode before the top encapsulation process. The tape was later removed after the top encapsulation process to expose the active contact area for electrical connection. A 50 μm-thick conductive tape (YCF50, Youngjin Co., LTD.), featuring a Cu-Ni-coated fabric backing and a conductive acrylic adhesive, was attached to the exposed active contact area as interconnection.

Fabrication of bottom and top encapsulation layers

The encapsulation layers of the device were fabricated using thermal ALD and spin coating, resulting in a 1.5 dyad organic-inorganic hybrid nano-stratified layer. In detail, the inorganic component was formed by thermal ALD, depositing a nano-stratified barrier composed of five sets of alternating 3 nm thick Al$_2$O$_3$ and ZnO layers. Al$_2$O$_3$ layers were produced using trimethylaluminum (TMA) and H$_2$O, while ZnO layers were created using diethylzinc (DEZ) and H$_2$O, all in a chamber maintained at 70 °C. The organic component, a SiO$_2$-polymer composite (i-OPTO BC 10, supplied by INTECH Nano Materials Co., Ltd, Korea), was applied using a spin coating and then thermally cured at 70 °C for 20 minutes to achieve a 300 nm thick layer. The encapsulation entailed applying the bottom layer to the PI substrate before the OLED layers were deposited and forming the top layer after the OLED deposition was completed.

Device characterization

The OLEDs were voltage-driven for device characterization by a source meter (Keithley 2400, Keithley Inc.), which simultaneously measured the current. The electroluminescence and wavelength spectra of the devices were recorded by a spectro-radiometer (CS-2000, Konica Minolta Inc.).

Data availability

The authors declare that the data supporting the findings of this study are available within the article and its Supplementary Information file. Additional data are available from the corresponding author upon request.

References

1. Srinivasan, R. & Mayne-Banton, V. Self-developing photoetching of poly(ethylene terephthalate) films by far-ultraviolet excimer lser radiation. *Appl. Phys. Lett.* **41**, 576–578 (1982).
2. Wang, F. et al. Laser lift-off technologies for ultra-thin emerging electronics: mechanism, applications, and progress. *Adv. Mater. Technol.* **8**, 2201186 (2023).
3. Bian, J. et al. Laser transfer, printing, and assembly techniques for flexible electronics. *Adv. Electron. Mater.* **5**, 1800900 (2019).
4. Choi, M.-C., Kim, Y. & Ha, C.-S. Polymers for flexible displays: from material selection to device applications. *Prog. Polym. Sci.* **33**, 581–630 (2008).
5. Park, C. I. et al. World's first large size 77-inch transparent flexible OLED display,. *J. Soc. Inf. Disp.* **26**, 287–295 (2018).
6. Park, J.-S. et al. Flexible full color organic light-emitting diode display on polyimide plastic substrate driven by amorphous indium gallium zinc oxide thin-film transistors. *Appl. Phys. Lett.* **95**, 013503 (2009).
7. Delmdahl, R., Patzel, R. & Brune, J. Large-area laser lift-off processing in microelectrnics. *Phys. Procedia* **41**, 241–248 (2013).
8. Jang, H.-W., Kim, S. K. & Yoon, S.-M. Impact of polyimide film thickness for improving the mechanical robustness of stretchable InGaZnO thin-film transistors prepared on wavy-dimensional elastomer substrates. *ACS Appl. Mater. Interfaces* **11**, 34076–34083 (2019).
9. Song, H. et al. Highly-integrated, miniaturized, stretchable electronic systems based on stacked multilayer network materials. *Sci. Adv.* **8**, eabm3785 (2022).
10. Lee, G.-H. et al. Multifunctional materials for implantable and wearable photonic healthcare devices. *Nat. Rev. Mater.* **5**, 149–165 (2020).
11. Cho, E. H. et al. Wearable and wavelength-tunable near-infrared organic light-emitting diodes for biomedical applications. *ACS Appl. Mater. Interfaces* **15**, 57415–57426 (2023).
12. Kim, H. et al. A flexible and wavelength-designable polymer light-emitting diode employing sandwich-encapsulation for wearable skin rejuvenation photomedicine. *Adv. Mater. Interfaces* **8**, 2100856 (2021).
13. Bian, J., Zhou, L., Yang, B., Yin, Z. & Huang, Y. A. Theoretical and experimental studies of laser lift-off of nonwrinkled ultrathin polyimide film for flexible electronics. *Appl. Surf. Sci.* **499**, 143910 (2020).
14. Kim, K., Kim, S. Y. & Lee, J.-L. Flexible organic light-emitting diodes using a laser lift-off method. *J. Mater. Chem. C.* **2**, 2144–2149 (2014).
15. Zhu, C., Guo, D., Ye, D., Jiang, S. & Huang, Y. A. Flexible PZT-integrated, bilateral sensors via transfer-free laser lift-off for multimodal measurements. *ACS Appl. Mater. Interfaces* **12**, 37354–37362 (2020).
16. Kim, S. J. et al. High-performance flexible thermoelectric power generator using laser multiscanning lift-off process. *ACS Nano* **10**, 10851–10857 (2016).
17. Kim, S. et al. Flexible crossbar-structured resistive memory arrays on plastic substrates via inorganic-based laser lift-off. *Adv. Mater.* **26**, 7480–7487 (2014).
18. Bian, J. et al. Experimental and modeling of controllable laser lift-off via low-fluence multiscanning of polyimide-substrate interface. *Int. J. Heat. Mass Transf.* **188**, 122609 (2022).

19. Kim, Y., Park, S., Kim, B.-K., Park, W.-J. & Kim, H. J. Laser lift-off of polyimide thin-film from glass carrier using DPSS laser pulses of top-hat sqaure profiles. *Opt. Laser Technol.* **142**, 107245 (2021).

20. Bae, S. et al. Roll-to-roll production of 30-inch graphene films for transparent electrodes. *Nat. Nanotechnol.* **5**, 574–578 (2010).

21. Balandin, A. A. Thermal properties of graphene and nanostructured carbon materials. *Nat. Mater.* **10**, 569–581 (2011).

22. Berman, D., Erdemir, A. & Sumant, A. V. Grpahene: a new emerging lubricant. *Mater. Today* **17**, 31–42 (2014).

23. Seif, M. A., Khashaba, U. A. & Rojas-Oviedo, R. Measuring delamination in carbon/epoxy composites using a shadow moire laser based imaging technique. *Compos. Struct.* **79**, 113–118 (2007).

24. Ferrari, A. C. et al. Raman spectrum of graphene and graphene layers. *Phys. Rev. Lett.* **97**, 187401 (2006).

25. Elbakoush, F. E. et al. Characterization and thermal degradiation study of carbonization the polyimide (PDMA/ODA)/Fe composite films. *Trans. Electr. Electron. Mater.* **22**, 843–850 (2021).

26. Kim, Y., Noh, Y., Park, S., Kim, B.-K. & Kim, H. J. Ablation of polyimide thin-film on carrier glass using 355 nm and 37 ns laser pulses. *Int. J. Heat. Mass Transf.* **147**, 118896 (2020).

27. Goyal, S. et al. Characterizing the fundamental adhesion of polyimide monomers on crystalline and glassy silica surfaces: a molecular dynamics study. *J. Phys. Chem. C* **120**, 23631–23639 (2016).

28. Min, K. et al. Interfacial adhesion behavior of polyimides on silica glass: a molecular dynamics study. *Polymer* **98**, 1–10 (2016).

29. Hong, J. et al. The mechanism study of laser peeling of ultra-thin polyimide film from the transparent substrate. *Surf. Interfaces* **36**, 102561 (2023).

30. Bian, J. et al. Laser-induced interfacial spallation for controllable and versatile delamination of flexible electronics. *ACS Appl. Mater. Interfaces* **12**, 54230–54240 (2020).

31. Kuper, S., Barnnon, J. & Brannon, K. Threshold behavior in polyimide photoablation: single-shot rate measurements and surface-temperature modeling. *Appl. Phys. A* **56**, 43–50 (1993).

32. Jeong, E. G. et al. A mechanically enhanced hybrid nano-stratified barrier with a defect suppression mechanism for highly reliable flexible OLEDs. *Nanoscale* **9**, 6370–6379 (2017).

33. Jeong, E. G., Kwon, J. H., Kang, K. S., Jeong, S. Y. & Choi, K. C. A review of highly reliable flexible encapsulation technologies towards rollable and foldable OLEDs. *J. Inf. Disp.* **21**, 19–32 (2020).

34. Jang, S. H. et al. Investigation of the chemical structure of ultra-thin polyimide substrate for the xenon flash lamp lift-off technology. *Polymers* **13**, 546 (2021).

35. Liu, W., Turkani, V. S., Akhavan, V. & Korgel, B. A. Photonic lift-off process to fabricate ultrathin flexible solar cells. *ACS Appl. Mater. Interfaces* **13**, 44549–44555 (2021).

36. Weidling, A. M., Turkani, V. S., Akhavan, V., Schroder, K. A. & Swisher, S. L. Large area photonic lift-off process for flexible thin-film transistors. *npj Flex. Electron.* **6**, 14 (2022).

37. Lee, S. I. et al. Xenon flash lamp lift-off technology without laser for flexible electronics. *Micromachines* **11**, 953 (2020).

38. Liu, J. et al. Thermal conductivity of giant mono- to few-layered CVD graphene supported on an organic substrate. *Nanoscale* **8**, 10298 (2016).

39. Kim, D.-H., Kim, B.-K., Kim, H. J. & Park, S. Crystallization of amorphous silicon thin-film on glass substrate preheated at 650 °C using Xe arc flash of 400 μs. *Thin Solid Films* **520**, 6581–6588 (2012).

40. Lee, W. et al. In-plane thermal conductivity of polycrystalline chemical vapor deposition graphene with controlled grain sizes. *Nano Lett.* **17**, 2361–2366 (2017).

41. Yung, W. K. C., Liu, J. S., Man, H. C. & Yue, T. M. 355 nm Nd:YAG laser ablation of polyimide and its thermal effect. *J. Mater. Process. Technol.* **101**, 306–311 (2000).

Author contributions

S.Kang and S.Kim conceived the research idea. S.Kang designed and performed the experiments, analyzes, and numerical simulations. J.C. conducted the experiments and analyzes related to OLED displays under the supervision of K.C.C. J.L. carried out the laser lift-off experiments under the supervision of S.Kim. D.J.K. assisted with the specimen preparation under the guidance of T.-S.K. S.Kang wrote the original draft and revised the manuscript. J.H.L. and S.Kim acquired the research funding. S.Kim supervised the project. All authors contributed to the discussion and review.

Competing interests

The authors declare no competing interests.

Additional information

Supplementary information The online version contains supplementary material available at https://doi.org/10.1038/s41467-024-52661-3.

Correspondence and requests for materials should be addressed to Seungman Kim.

Peer review information *Nature Communications* thanks the anonymous reviewers for their contribution to the peer review of this work. A peer review file is available.

Reprints and permissions information is available at http://www.nature.com/reprints

Publisher's note Springer Nature remains neutral with regard to jurisdictional claims in published maps and institutional affiliations.